remote sensing

Article

Automatic Crest Line Extraction Algorithm for Internal Solitary Waves Based on SWOT

Pengyi Chen [1,†], Jiannan Gao [1,†], Jinlong Huang [1], Longyu Jiang [1], Yu Huang [1], Rui Xuan [1], Yiyang Li [1], Yang Chen [1], Bangxin Zheng [1], Hangyu Zhou [2], Shaojie Guo [1], Xiangyu Ren [1] and Xuejun Xiong [1,*]

[1] Institute of Physical Oceanography and Remote Sensing, Ocean College, Zhejiang University, Zhoushan 316000, China; 22434197@zju.edu.cn (P.C.); 12434096@zju.edu.cn (J.G.); 12534121@zju.edu.cn (J.H.); 25jianglongyu@zju.edu.cn (L.J.); 12534048@zju.edu.cn (Y.H.); 12534122@zju.edu.cn (R.X.); 3210104146@zju.edu.cn (Y.L.); 22534190@zju.edu.cn (Y.C.); 12434121@zju.edu.cn (B.Z.); 22534195@zju.edu.cn (S.G.); l232131@zju.edu.cn (X.R.)

[2] Division of Biosciences, Faculty of Life Sciences, University College London, London WC1E 6BT, UK; ucbthz1@ucl.ac.uk

* Correspondence: xiongxj@zju.edu.cn

† These authors contributed equally to this work.

Highlights

What are the main findings?

- A label-free ISW crest line segmentation workflow for SWOT L3 LR Unsmoothed SSHA is developed using Gaussian scale separation and morphology-constrained filtering.
- Our algorithm remains robust under 4 challenging conditions: typhoon/rain, strong striping noise, shallow-shelf weak signals, and multi-wave interference.

What are the implications of the main findings?

- The framework enables reproducible, sample-efficient ISW crest extraction from 2-D SSHA without requiring pixel-level training datasets.
- Reliable crest delineation supports SWOT-based retrieval of ISW dynamical parameters.

Abstract

Sea surface height anomaly (SSHA) observations from Surface Water and Ocean Topography (SWOT) provide a new opportunity for identifying crest lines of internal solitary waves (ISWs). However, L3 LR Unsmoothed SSHA is often affected by residual large-scale trends, rainfall contamination, and stripe noise, which limit segmentation performance. To address this issue, we propose an automatic segmentation workflow for SWOT SSHA. The workflow first applies Gaussian low-pass filtering for scale separation to extract high-frequency SSHA, then uses Otsu adaptive thresholding to segment ISW signals, and finally removes false targets using morphological geometric constraints. Validation based on 230 SWOT images from the northern South China Sea shows that, compared with the conventional method based on subtracting reanalysis fields, the proposed method increases the contrast-to-noise ratio (CNR) of high-frequency SSHA by 1.35 on average (Std = 0.99) and improves signal gain by 13.65 dB on average (Std = 7.71 dB). The method remains robust under complex conditions, including strong typhoons, severe stripe noise, weak shelf signals, and multi-wave interference. In some cases, quasi-synchronous optical imagery further confirms the authenticity of the extracted crest lines.

Check for updates

Academic Editor: Andrea Storto

Received: 20 March 2026
Revised: 26 April 2026
Accepted: 1 May 2026
Published: 7 May 2026

Keywords: SWOT; internal solitary wave; image segmentation; morphological constraints; northern South China Sea

1. Introduction

Internal solitary waves (ISWs) are strongly nonlinear, large-amplitude, short-period disturbances that develop within stably stratified seawater and affect nearly the entire ocean water column [1]. During propagation and breaking, ISWs can induce intense water mixing, transferring upper-ocean energy downward while transporting deep chlorophyll, nutrients, and other materials upward. They therefore enhance marine photosynthesis, increase primary productivity, and influence marine ecosystems [2–4]. The northern South China Sea (SCS) is one of the most active regions for ISWs worldwide [5,6]. Previous studies have shown that ISWs in the northern SCS are commonly generated by interactions between tidal currents and steep topography near the Luzon Strait [7]. They then propagate westward across the deep basin with substantial energy and eventually dissipate over the continental shelf [8,9]. At present, observations of ISWs mainly rely on in situ measurements and remote sensing. Compared with conventional observations, remote sensing offers broad spatial coverage, all-time and all-weather capability, and high resolution, and has therefore been widely used in ISW studies in different oceanic regions [10]. Early remote sensing studies of ISWs mainly relied on synthetic aperture radar (SAR) and optical satellites. As ISWs propagate, they induce convergence and divergence in the surface flow field and modify sea surface roughness, producing alternating bright and dark banded patterns in SAR imagery [11–13]. Optical satellites mainly detect ISW-induced roughness changes through sunglint reflected from the sea surface [14]. However, both SAR and optical imagery are constrained by observing conditions. SAR is sensitive to wind and sea state [15–17], whereas optical imagery is easily affected by cloud cover and illumination conditions [18–22]. Moreover, the imaging mechanisms of both methods mainly depend on ISW-induced roughness variations, making it difficult to directly quantify sea surface height disturbances that are closely linked to wave dynamics, which limits their application in ISW detection. In contrast, altimeters provide more direct observations of sea surface height and can capture ISW-induced disturbances from centimeters to decimeters in along-track sea surface height anomaly (SSHA) [23,24]. However, conventional altimeters are limited by one-dimensional along-track sampling and cannot resolve the two-dimensional SSHA signatures of ISW crest lines.

The launch of the Surface Water and Ocean Topography (SWOT) mission has made two-dimensional SSHA observations of ISWs possible [25]. Its Ka-band interferometric radar provides SSHA measurements at 250 m resolution over two 50 km swaths on either side of the nadir track, enabling SWOT to detect a wide range of submesoscale features, including internal waves [26,27]. Recent studies have used SWOT SSHA to retrieve ISW dynamic parameters [28–31], and band-pass filtering has also been applied to extract ISW crest lines for analyzing how mesoscale eddy–ISW interactions affect crest line morphology [32]. Robust segmentation of ISW crest lines in SWOT data is therefore fundamental to retrieving ISW dynamic parameters from SSHA and to investigating their interactions with other ocean dynamical processes. For a long time, segmentation of ISW crest lines in remote sensing imagery has mainly relied on traditional image processing methods and deep learning methods. In traditional image processing, Rodenas et al. used a two-dimensional discrete wavelet transform to segment ISW crest lines from low-signal-to-noise-ratio SAR images [33], whereas Zheng et al. used the Canny operator for edge detection and achieved segmentation of ISW boundaries [34]. In deep learning, U-Net was adopted early for ISW segmentation [35], and was followed by dedicated models and attention mechanisms developed specifically for this task [36–38]. Compared with traditional image processing methods, deep learning has stronger generalization ability in low-signal-to-noise-ratio conditions or in scenes influenced by multiple overlapping dynamical processes. However, most existing ISW segmentation models are supervised and require a large number of labeled samples for training. For SWOT data, no dataset is yet available for direct use in ISW segmentation. This study therefore combines Gaussian filtering with morphological algorithms to segment ISWs in the SWOT SSHA fields.

Beyond image segmentation itself, robust extraction of ISW crest lines from SWOT SSHA is also important for oceanographic applications. Accurate crest delineation provides a geometric basis for characterizing wavefront orientation, curvature and continuity, and therefore supports the interpretation of ISW generation, propagation, refraction, diffraction, and interaction with background circulation and topography. In this sense, extracting crest lines from 2D SWOT SSHA is not only an image-processing task, but also a key foundation for SWOT-based observation and dynamical analysis of internal solitary waves.

To address the difficulty of robustly extracting ISW crest lines from SWOT SSHA under strong background trends and complex noise conditions, this study proposes an automatic segmentation method that combines Gaussian filtering with morphological constraints. First, a Gaussian low-pass filter is used to estimate the low-frequency background field in SWOT observations, and this background is subtracted from the original data to obtain high-frequency SSHA, thereby enhancing ISW crest line textures. Candidate internal wave regions are then identified using the Otsu adaptive threshold, and the resulting targets are further screened by morphological geometric metrics, including connected-component area, major-axis length, and aspect ratio, to suppress false detections caused by speckle noise and improve algorithm reliability. In addition, the method is quantitatively evaluated in terms of the contrast-to-noise ratio (CNR) and signal gain, and is compared with a conventional high-frequency extraction baseline to verify its reliability in extracting ISW crest lines under different dynamical environments and extreme noise conditions.

The remainder of this paper is organized as follows. Section 2 introduces the SWOT SSHA product and describes the preprocessing procedure, high-frequency component extraction method, and morphological algorithm used in this study. Section 3 presents the results after Gaussian filtering and morphological processing, and demonstrates the performance of the proposed method for ISW segmentation in different ocean regions. Section 4 first analyzes the sensitivity of Gaussian filtering, then compares the proposed method with conventional high-frequency SSHA extraction methods, and finally discusses the authenticity of the extracted crest lines. Section 5 summarizes the study.

2. Materials and Methods

2.1. Data

This study used SWOT data acquired along the 21-day repeat orbit and collected a total of 243 SWOT Unsmoothed L3_LR_SSH products (version 2.0.1). The observations span from March 2024 to March 2025 and cover the northern SCS, within 113°E–122°E and 18°N–24°N. This product includes several key variables, such as unedited SSHA, normalized radar cross section (NRCS), and quality flags, and the meanings of the quality indicators are listed in Table 1.

Because ISWs in SWOT SSHA images usually appear as pronounced positive anomalies that deviate markedly from the local mean background, directly removing pixels flagged as 5 or 30 may incorrectly discard real internal wave signals. This study therefore retained pixels with flags of 0, 5, and 30 during the initial quality control. After this initial screening, 230 of the 243 products contained valid data. Figure 1 shows the quality-controlled SWOT SSHA data for three consecutive days from 11 to 13 March 2024. The observation sequence captures the life-cycle evolution of ISWs, from their generation near the boundary between the deep basin and the Luzon Strait, to northwestward propagation and nonlinear steepening over the continental slope, and finally to shoaling deformation and dissipation over the continental shelf west of the Dongsha Atoll, corresponding to regions A, B, and C.

Table 1. SWOT L3 quality flag.

Flag	Quality Flag
102	Defaulted SSHA values.
101	Pixels over land using a mask.
100	Swath edge pixels if the KaRIn Level 2 quality bit 256 is raised.
70	Pixels impacted by spacecraft events.
50	Abnormally high SSHA values in coastal and polar regions.
30	SSHA pixels that are out of the expected statistical distribution.
20	Suspected sea ice pixels.
19	Unsure sea-ice pixels.
18	Unsure ocean pixels in polar areas
10	Suspected coastal pixels.
5	Pixels that deviate from a locally smoothed version of the SSHA.
3	Eclipses
0	Valid data

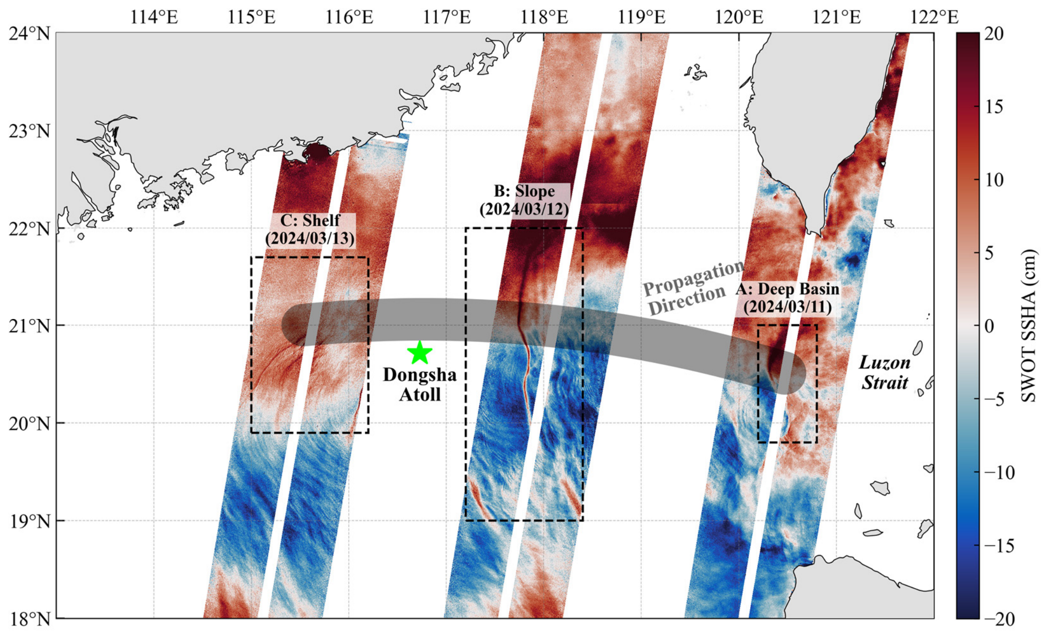

Figure 1. The quality-controlled SWOT SSHA data acquired on three consecutive days from 11 to 13 March 2024. The right, middle, and left swaths correspond to the observations on 11, 12, and 13 March, respectively. The dashed boxes indicate the three representative regions discussed in the main text.

To compare with the method proposed in a previous study [30], in which high-frequency components were extracted by subtracting reanalysis SSHA from SSHA, this study used the "Global Ocean Gridded L4 Sea Surface Heights and Derived Variables Nrt" product released by the Copernicus Marine Service. This Level-4 product is generated from along-track observations of multiple satellite altimeters, including Sentinel-3 and Jason-3, using optimal interpolation to produce seamless gridded data, with a spatial resolution of 0.125° × 0.125°, and a daily temporal resolution. Because this product has undergone spatiotemporal smoothing and mainly reflects large-scale ocean circulation and mesoscale eddy features, it was used as the background field for reproducing the baseline method.

In addition, the significant wave height (SWH) used for sea-state discussions is obtained from ERA5 post-processed daily statistics. It should be noted that the SWOT L3 LR product has already applied sea-state bias (SSB) correction, but residual sea-state-related uncertainties may still affect the quality of the obtained high-frequency SSHA fields and their segmentation performance.

2.2. Image Preprocessing

The image-processing workflow mainly consists of three steps, including preprocessing, high-frequency component extraction, and image segmentation. Each step is introduced in turn below. In the preprocessing stage, pixels with quality flags other than 30, 5, and 0 are first assigned NaN values to reduce the influence of abnormal pixels on SSHA. The mask obtained after this quality-control step is then subjected to five successive binary erosions, and the processed mask is subsequently applied to SSHA. The expression for the successive binary erosion is given by Equation (1).

$$\begin{cases} A_0 = A \\ A_k = A_{k-1} \ominus B \quad k = 1, \ldots, N \end{cases} \tag{1}$$

Here, A denotes the SSHA mask obtained after the previous quality-control step, B denotes a 3×3 cross-shaped structuring element, N denotes the number of successive erosions, and $\ominus$ denotes the morphological image erosion operator, whose definition is given by Equation (2).

$$A \ominus B = \{z \in E | (B)_z \subseteq A\} \tag{2}$$

Figure 2 shows the spatial distribution of SSHA in a SWOT image near Hong Kong Island on 26 March 2024, before and after successive erosion processing. Figure 2a presents the original unprocessed data and reveals clear land-signal contamination near the narrow channel between the Kowloon Peninsula and Hong Kong Island, as well as along the complex coastline, appearing as extreme anomalies greater than 1 m or less than -1 m. Figure 2b shows the result after five successive morphological erosions. The comparison indicates that this method effectively removes nearshore pixels contaminated by land echoes, substantially suppresses spurious high-frequency noise associated with the coastline, and leaves anomalies only in a few offshore areas, thereby providing a reliable basis for subsequent high-frequency signal extraction.

Subsequently, a 3×3 mean filter and a 50×50 blockwise threshold filter were applied sequentially to the SSHA image to suppress high-frequency random noise. The blockwise thresholding procedure is given in Equations (3) and (4).

$$\mu_{m,n} = \text{nanmean}(B_{m,n}) = \frac{1}{K} \sum_{(x,y) \in B_{m,n}, S_{x,y} \neq \text{NaN}} S_{x,y} \tag{3}$$

$$S_{x,y}^{\text{new}} = \begin{cases} \text{NaN}, & \text{if } |S_{x,y} - \mu_{m,n}| > \tau \\ S_{x,y}, & \text{otherwise} \end{cases} \tag{4}$$

Here, $u_{m,n}$ denotes the mean of non-NaN pixels within block $B_{m,n}$, $B_{m,n}$ denotes the block at row m and column n, $S_{x,y}$ denotes the pixel value at row x and column y in the SSHA image, K denotes the number of non-NaN pixels in that block, and τ denotes the prescribed threshold, which was set to 0.5 m in this study. Finally, pixels with absolute SSHA values greater than 1 m were removed.

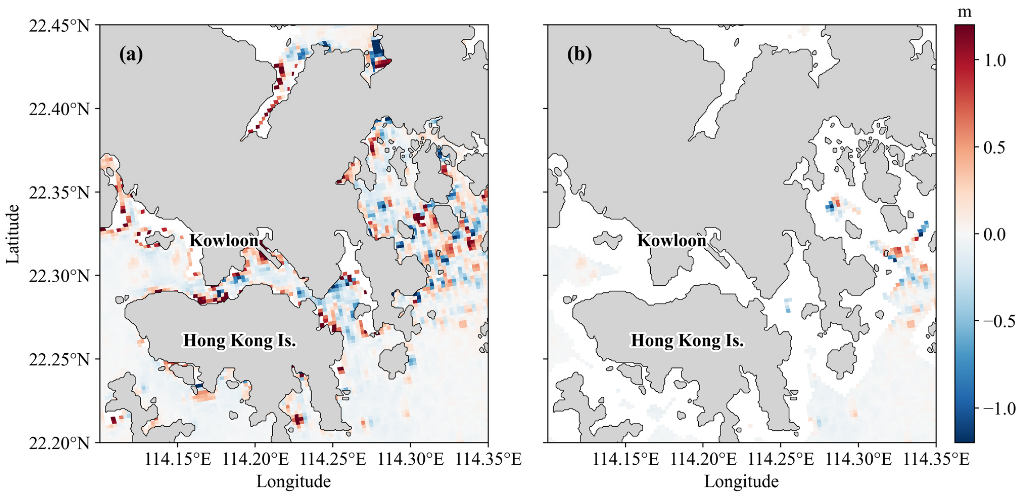

Figure 2. (**a**) SSHA before successive erosion and (**b**) SSHA after five successive erosions.

2.3. High-Frequency Component Extraction of SSHA

In the high-frequency component extraction stage, a Gaussian filter with $\sigma = 20$ was first applied to the SSHA image. The two-dimensional Gaussian kernel in the spatial domain is given by Equation (5).

$$G(x,y) = \frac{1}{2\pi\sigma^2} e^{-\frac{x^2+y^2}{2\sigma^2}} \tag{5}$$

and its frequency-domain representation is given by Equation (6).

$$G(u,v) = e^{-2\pi^2\sigma^2(u^2+v^2)} \tag{6}$$

Here, x, y denote the coordinate distances of a pixel relative to the kernel center, which is usually set at (0, 0), σ denotes the standard deviation, and u, v denote the frequency-domain coordinates.

Figure 3 shows the spatial-domain distribution of the two-dimensional Gaussian kernel with $\sigma = 20$, together with the amplitude distribution of its two-dimensional Fourier transform in the frequency domain. The results indicate that the Gaussian kernel is essentially a low-pass filter with a cutoff frequency of $D_0 = 1/(2\pi\sigma)$. The low-frequency component of SSHA can be extracted by convolving the SSHA image with this kernel in two dimensions. Subtracting this low-frequency component from the original SSHA then yields the high-frequency component and effectively removes the background trend.

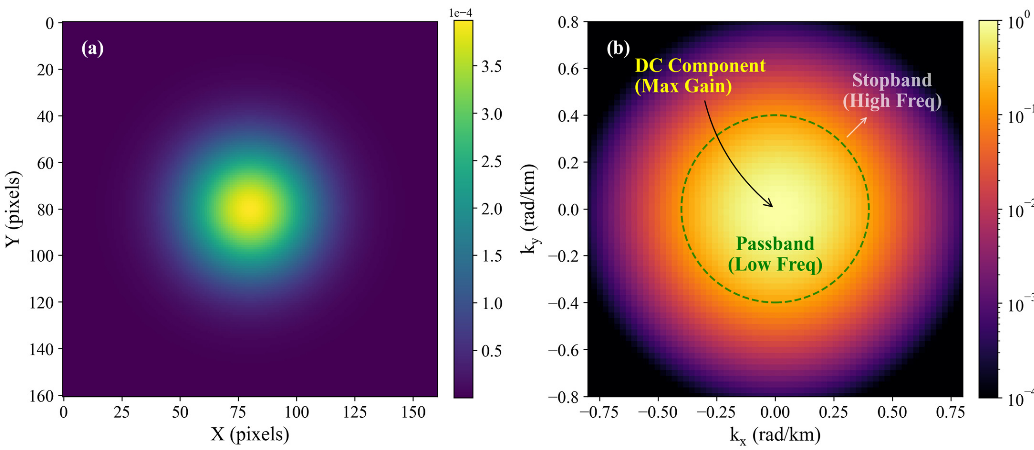

Figure 3. (**a**) Spatial-domain distribution of the two-dimensional Gaussian filter kernel and (**b**) Amplitude distribution of the two-dimensional Gaussian filter kernel in the frequency domain.

2.4. ISW Stripe Segmentation

In the image segmentation stage, global grayscale histogram clipping was first applied to SSHA, retaining only pixels within the 10–100% intensity range, while all other pixels were set to NaN. A 3×3 mean filter was then applied, and global and local Otsu methods were combined to segment ISW bands. Otsu's method is an adaptive threshold-based binary segmentation approach whose core idea is to traverse candidate thresholds and maximize the between-class variance between the foreground and background [19], as expressed in Equation (7).

$$\sigma_B^2(\tau) = w_{fg}(\tau) \cdot w_{bg}(\tau) \cdot [\mu_{fg}(\tau) - \mu_{bg}(\tau)]^2 \tag{7}$$

Here, $w_{fg}(\tau)$ and $w_{bg}(\tau)$ denote the numbers of foreground and background pixels, respectively, whereas $\mu_{fg}(\tau)$ and $\mu_{bg}(\tau)$ denote the mean gray values of the foreground and background, respectively. Because SSHA values of ISW pixels are usually markedly higher than those of the background, Otsu's method is well suited for ISW segmentation. In this study, the local Otsu threshold was calculated within a 50×50 pixel sliding window to accommodate spatial variations in SSHA contrast, whereas the global Otsu threshold provided an overall constraint to suppress background noise introduced by locally high-sensitivity regions and to ensure the consistency and reliability of the segmentation results across the entire swath.

In addition to conventional adaptive threshold segmentation, this study further incorporated morphological constraints into the screening of segmentation results. Previous studies have shown that ISW crest lines in SWOT images usually appear as arc-shaped bands and predominantly propagate northwestward. Based on this characteristic, a PCA-based filtering method was developed to screen objects by their oblique orientation and aspect ratio. Specifically, individual connected components were first extracted from the segmented mask using the four-connectivity criterion shown in Figure 4. For each connected component, the coordinate vector of each pixel, $(x, y)^T$ was mean-centered by subtracting $(\overline{x}, \overline{y})^T$, yielding the centered coordinate $\widetilde{\mathbf{p}}_i = (\widetilde{x}, \widetilde{y})^T$. The sample covariance matrix of the centered data was then calculated, as given in Equation (8).

$$\Sigma = \frac{1}{N-1} \sum_{i=1}^{N} \widetilde{\mathbf{p}}_i \widetilde{\mathbf{p}}_i^T = \begin{bmatrix} \mathrm{Var}(x) & \mathrm{Cov}(x, y) \\ \mathrm{Cov}(y, x) & \mathrm{Var}(y) \end{bmatrix} \tag{8}$$

Here, N denotes the number of sample points, $\mathrm{Var}(x)$ denotes the variance of row coordinates, and a larger value indicates a broader vertical distribution of the connected component. $\mathrm{Var}(y)$ denotes the variance of column coordinates, and a larger value indicates a broader horizontal distribution. $\mathrm{Cov}(x, y)$ denotes the covariance between row and column coordinates. A positive value indicates a left-upper to right-lower tilt of the connected component, a negative value indicates a right-upper to left-lower tilt, and a value of zero indicates no clear correlation between row and column variations.

By performing eigen decomposition of the covariance matrix Σ, the characteristic equation can be obtained as shown in Equation (9).

$$\Sigma \mathbf{v} = \lambda \mathbf{v} \tag{9}$$

This yields two eigenvalues, λ_1, λ_2, together with their corresponding unit eigenvectors, $\mathbf{v}_1, \mathbf{v}_2$. With $\lambda_1 \geq \lambda_2$, the associated eigenvectors are defined as the principal-direction vector $\mathbf{v}_{\mathrm{major}}$ and the minor-direction vector $\mathbf{v}_{\mathrm{minor}}$, respectively. The centered point set $\widetilde{P}$ is then projected onto the principal and minor directions. For each point $\widetilde{\mathbf{p}}_i$, the projection coordinates on the major and minor axes, $y_{i,major}, y_{i,minor}$, are given in Equation (10).

$$\begin{cases} y_{i,major} = \widetilde{\mathbf{p}}_i^T \cdot \mathbf{v}_{major} \\ y_{i,minor} = \widetilde{\mathbf{p}}_i^T \cdot \mathbf{v}_{minor} \end{cases} \tag{10}$$

The major- and minor-axis lengths L_{major} and L_{minor} are further calculated using Equation (11), and the aspect ratio R is defined by Equation (12) using the connected-component area A.

$$\begin{cases} L_{major} = \max(y_{i,major}) - \min_i(y_{i,major}) \\ L_{minor} = \max(y_{i,minor}) - \min(y_{i,minor}) \end{cases} \tag{11}$$

$$R = \frac{L_{\mathrm{major}}^2}{A} \tag{12}$$

By removing connected components that satisfy $R < 6.0$, $L_{major} < 100$ or $A < 300$, false targets produced by threshold-based segmentation can be eliminated, yielding the morphologically filtered ISW mask.

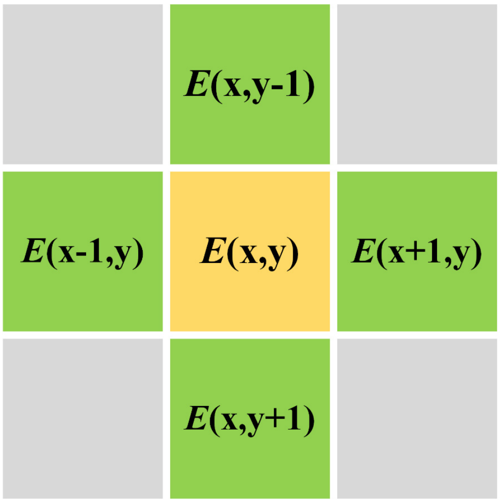

Figure 4. Schematic illustration of four-connectivity. The yellow, green, and gray cells indicate the central pixel, four-connected neighboring pixels, and non-connected diagonal pixels, respectively.

2.5. Workflow of ISW Stripe Segmentation

The overall workflow of the proposed algorithm is shown in Figure 5. It consists of three main modules: preprocessing, high-frequency component extraction, and ISW segmentation. In the preprocessing stage, the original SWOT SSHA data are sequentially subjected to quality control, coastal-edge erosion, 3×3 mean filtering, block-wise mean filtering, and removal of anomalous values greater than 1 m to reduce noise contamination and eliminate invalid pixels. In the high-frequency component extraction stage, a Gaussian filter with $\sigma = 20$ is applied to obtain the low-frequency SSHA component, and the high-frequency SSHA component is then derived by subtracting the low-frequency component from the original SSHA. In the ISW segmentation stage, global grayscale histogram clipping is first used to reduce the influence of extremely low-SSHA pixels on segmentation, after which block-wise Otsu thresholding and global Otsu thresholding are combined to extract candidate ISW signals. Finally, geometric constraints based on area, major-axis length, and aspect ratio are used to remove small connected regions and non-target structures, yielding the final ISW mask. Overall, this workflow integrates multilevel denoising, scale separation, and morphological screening, thereby improving the identification of slender ISW signals in SWOT observations.

https://doi.org/10.3390/rs18101463

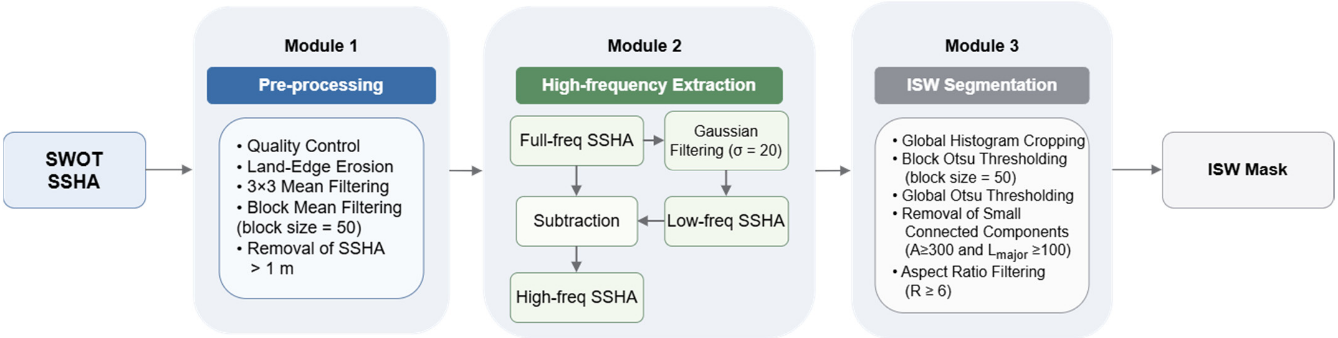

Figure 5. Overall workflow of the proposed algorithm.

3. Results

3.1. Results of High-Frequency SSHA Extraction

To evaluate the robustness of the proposed high-frequency SSHA extraction algorithm under complex ocean dynamical conditions, this study selected a representative SWOT SSHA image acquired on 26 July 2024, as a case study. The image covers the waters surrounding Dongsha Atoll in the northeastern SCS. This region is not only one of the most active areas for ISWs in the SCS, but also a typical region where internal waves are strongly coupled with mesoscale eddies and large-scale background flows such as sea surface tilts. Therefore, this complex scene, which contains both strong background interference and ISW signals, provides a representative test case for assessing the detrending capability of the high-frequency SSHA extraction algorithm.

Figure 6 presents the separation results of the large-scale background field and the high-frequency SSHA signal in SWOT observations. Figure 6a shows the preprocessed SSHA, in which high-frequency bands induced by ISWs are superimposed on a pronounced low-frequency background. Figure 6b shows the reanalysis SSHA on the same day, and Figure 6c shows the low-frequency component obtained by applying a Gaussian low-pass filter with $\sigma = 20$ to Figure 6a. This component represents the large-scale background field dominated by processes such as mesoscale circulation and sea surface tilt. A comparison between Figures 6b and 6c shows good agreement in both spatial pattern and amplitude scale. Both exhibit positive anomalies in the south and negative anomalies in the north, and their overall scales are also similar. Meanwhile, as an internally derived scale-separation result from SWOT observations, Figure 6c preserves background structural information at higher spatial resolution while maintaining the same large-scale morphology as the reanalysis. This consistency indicates that the Gaussian low-pass filtering used here can reasonably characterize the low-frequency background component in SWOT observations and provide a self-consistent background reference for constructing the high-frequency SSHA residual field. For high-frequency signal extraction, Figure 6d shows the difference residual obtained by using the reanalysis field as the background reference, namely Figure 6a minus Figure 6b. Because the low-frequency signal in the reanalysis product does not fully match the low-frequency background in SWOT SSHA, the difference field still retains a visible large-scale trend, indicating that background removal is incomplete. By contrast, Figure 6e shows the high-frequency component obtained with the Gaussian filtering method, namely Figure 6a minus Figure 6c. This result effectively suppresses the low-frequency background, brings the regional mean SSHA closer to zero, and more completely preserves the fine-scale crest textures and edge-gradient features of ISW trains, thereby substantially improving the signal-to-noise ratio and structural discriminability required for subsequent segmentation and morphological classification.

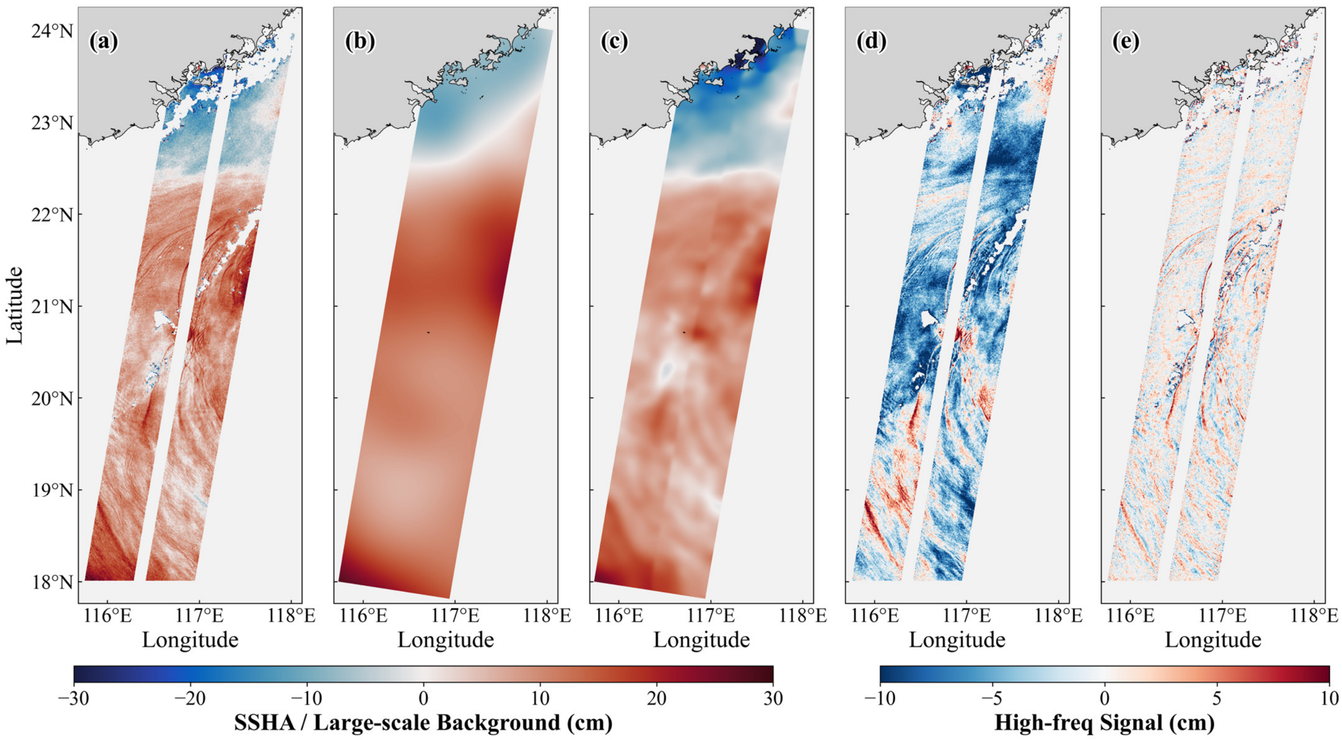

Figure 6. (**a**) Preprocessed SSHA, (**b**) reanalyzed SSHA on the same day, (**c**) the low-frequency SSHA component extracted by Gaussian filtering, (**d**) the high-frequency component obtained by removing the reanalyzed field from the preprocessed SSHA, and (**e**) the high-frequency component obtained by removing the low-frequency component from the preprocessed SSHA.

3.2. Morphology-Constrained ISW Segmentation Performance

Figure 7 presents an example of ISW signal segmentation over the shelf region from SWOT observations on 13 March 2024. The band is located in a shallow shelf environment, where the amplitude of the internal solitary wave in the high-frequency SSHA component is generally small, at about 2 cm, and the crest line is also narrow, approaching the effective spatial resolution of 250 m in the SWOT Unsmoothed product. At this sampling interval, the minimum resolvable scale corresponding to the spatial Nyquist wavenumber is about 500 m. When the ISW crest line width falls within the sub-kilometer range, it is represented by only a few pixels in the gridded field and is therefore easily affected by the 3×3 mean filter applied in preprocessing, leading to a narrow and discontinuous appearance. This weakens the spatial coherence of the crest line and increases the probabilities of missed detections and false detections in threshold-based segmentation, as shown in Figure 7a. In SWOT SSHA images with a low signal-to-noise ratio and interference among multiple crest lines, the spatial coherence of crest lines is further reduced. As a result, wave-train structures are more likely to become discontinuous or fragmented, or to be mixed with noise textures, making it difficult for purely threshold-based methods to stably identify real ISW crest lines.

In Figure 7b, the result of pure Otsu threshold segmentation is shown by red pixels and produces a large number of scattered connected components and speckle-induced false detections over the shelf region. By contrast, the morphologically filtered result, shown by green pixels, substantially suppresses these speckle noises and scattered connected components, retaining only internal wave band structures with typical geometric characteristics. This screening process identifies candidate targets using morphological features such as connected-component area, aspect ratio, and major-axis length. Figure 7c further shows that real internal wave crest lines usually correspond to slender connected components with a larger major-axis length and higher aspect ratio, whereas noise-induced false targets are more likely to appear as small scattered structures with a limited area, short major axis, or near-isotropic shape. Therefore, by imposing joint constraints on these geometric parameters, namely a major-axis length of at least 100 pixels, an aspect ratio of at least 6, and a connected-component area of at least 300 pixels, the morphological algorithm can effectively distinguish elongated crest bands from random noise patches without relying on any external background field. Cross-sectional validation further demonstrates that morphological constraints improve segmentation reliability. Along the normalized section from A to B in Figure 7a, shown in Figure 7d, the ISW signals identified by pure Otsu segmentation are marked by red shading and frequently misclassify weak undulations and noise fluctuations as targets at multiple locations. In contrast, the results retained after morphological screening are marked by green shading and are more concentrated in signal segments that correspond to ISW bands and exhibit consistent structural scale and spatial continuity, thereby improving the robustness of ISW identification under weak-amplitude, narrow-width, and low-signal-to-noise-ratio conditions over the shelf region.

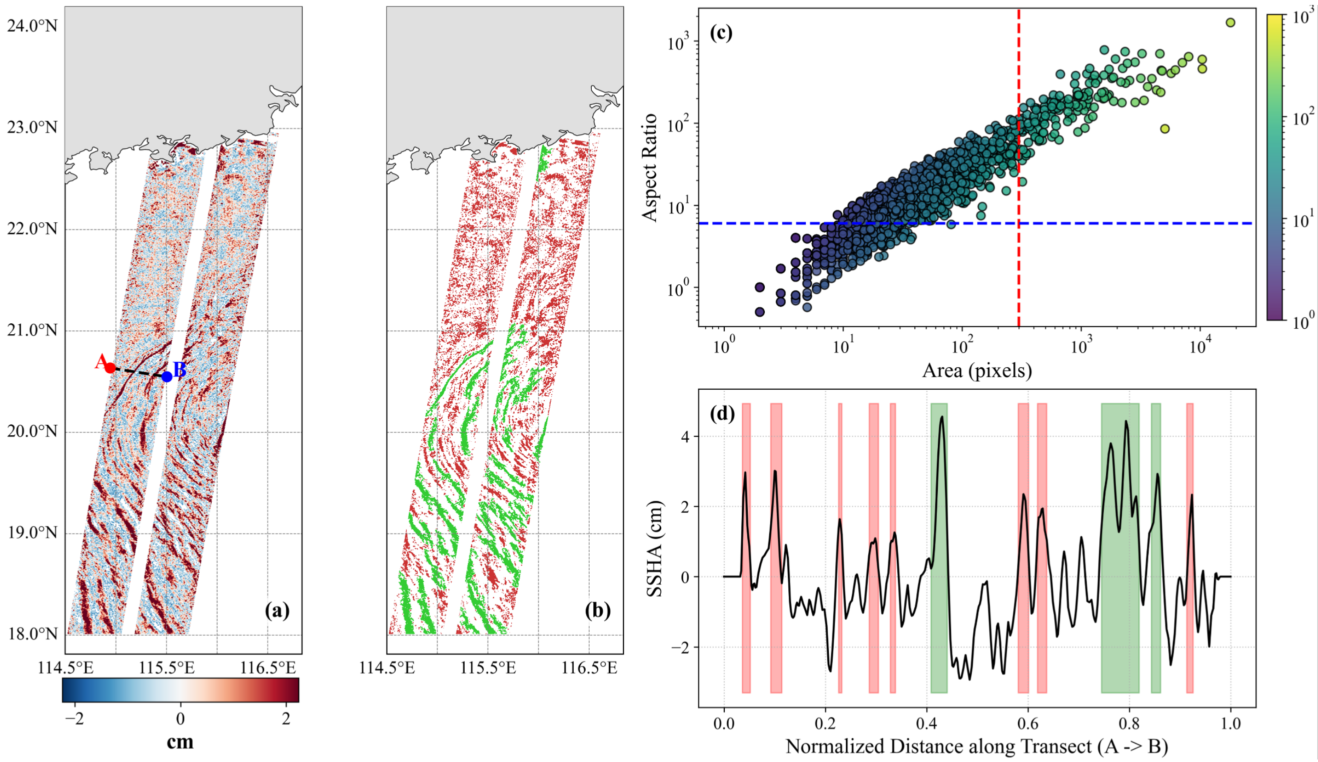

Figure 7. (**a**) Spatial distribution of the high-frequency SSHA component where the black dashed line marks the A–B transect used for the cross-sectional analysis in panel (**d**), (**b**) ISW segmentation results, with red pixels showing the Otsu result and green pixels showing the ISW signals retained by the morphological algorithm, (**c**) relationship of connected-component area and aspect ratio with major-axis length, where the blue line marks the aspect-ratio threshold of 6 and the red line marks the area threshold of 300, and (**d**) section from Point A to Point B in panel (**a**), with the red shaded area showing the Otsu result and the green shaded area showing the retained ISW signal.

3.3. Identification of ISW from SWOT SSHA Image

To evaluate the applicability of the SWOT-image-based ISW segmentation algorithm under different topographic and dynamical conditions, this study analyzed the three SWOT SSHA images shown in Figure 1, acquired on three consecutive days from 11 to 13 March 2024. These images cover three representative regions in the northern SCS, namely the ISW generation zone near the boundary between the Luzon Strait and the deep basin, the ISW propagation and nonlinear steepening zone near the boundary between the continental slope and the deep basin, and the ISW shoaling and dissipation zone west of the Dongsha Islands. The SWOT observation on 11 March 2024 covers the Luzon Strait, a key region for internal wave generation, corresponding to the right-hand swath in Figure 8. Unlike the regular, long arc-shaped wavefronts seen in the deep basin, the high-frequency SSHA field in this region contains many short, discontinuous, and highly fragmented crest lines. From the perspective of physical evolution, this morphology indicates that nonlinear steepening and fission of ISWs in this region are still incomplete, and the crest lines have not yet fully evolved into isolated soliton-like structures. In addition, strong background-flow shear and topographic scattering in the near-source region further enhance wavefront bending and fragmentation. Even so, the Gaussian-filtering and morphological-extraction framework proposed here can still accurately capture these early-stage ISWs and effectively avoid merging adjacent interference stripes into blurred clusters, thereby enabling a refined decomposition of complex near-field coherent structures.

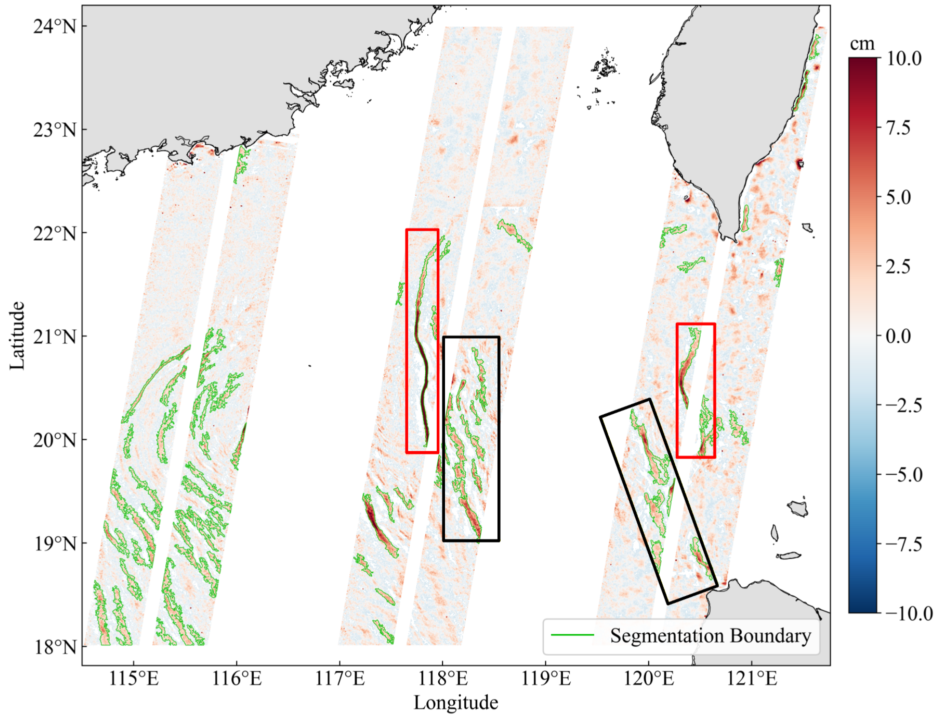

Figure 8. High-frequency SSHA component, with green outlines indicating the segmented ISW boundaries. Crest lines within the black box correspond to ISWs originating from the Babuyan Islands, whereas those within the red box correspond to ISWs originating from the ridge east of Luzon Strait.

As ISWs propagated westward into the deep basin, the high-frequency SSHA field on 12 March (the middle swath in Figure 8) exhibited typical wave-packet characteristics of ISWs. The crest lines were dominated by continuous, arc-shaped, and long-distance banded structures, with markedly enhanced spatial coherence, and were followed by trailing wave trains with a progressively decreasing amplitude. These features are consistent with the classical understanding that ISWs in the northern SCS evolve gradually from internal tides into soliton trains. The proposed algorithm showed excellent continuity in crest line extraction at this stage. In particular, within the red rectangular region in the middle swath, the algorithm successfully extracted complete crest lines extending over more than 100 km without obvious physical breaks or artifact contamination, indicating that it can accurately capture large-scale coherent structures under high signal-to-noise-ratio conditions. More importantly, the crest lines identified on 12 March can be clearly linked to those observed on 11 March from different source regions. The crest lines within the black polygon are identified as ISWs originating from the Babuyan Islands in the southern Luzon Strait, and in the 12 March image, they appear as wave-train structures located in the southern part of the swath, with a relatively consistent orientation and a fan-shaped spreading pattern. By contrast, the crest lines within the red rectangle correspond to ISWs originating from the ridge east of the Luzon Strait. As these ISWs propagated westward away from the source region, they gradually became dominant and evolved into a more continuous and coherent arcuate leading wavefront.

When ISWs propagate into the Dongsha Atoll region, their wavefronts undergo pronounced refraction under the strong modulation of rapidly shoaling topography and split into two sub-wave packets that evolve southward and northward, respectively. The observation on 13 March, corresponding to the left-hand swath in Figure 8, shows the SSHA distribution associated with the crest lines of the southern branch. The image reveals two prominent features in this region: wavefront refraction induced by shallow topography and wave-packet fission, in which the leading wave further breaks into a train of high-frequency solitons. Under these complex dynamical conditions, the algorithm still exhibits good separability. It can not only accurately delineate the strongly curved wavefronts produced by refraction, but it can also isolate individual solitons that are closely packed within the fissioned wave packet, indicating that the algorithm maintains high geometric fidelity when dealing with fragmented structures generated by nonlinear evolution.

4. Discussion

4.1. Sensitivity Analysis of Standard Deviation for Gaussian Filter Kernel

Gaussian filtering for extracting the high-frequency SSHA component is a key step before adaptive-threshold segmentation. To quantitatively assess the effect of filter scale on ISW segmentation, this study selected a SWOT SSHA image acquired on 8 July 2024 and compared the extracted high-frequency SSHA components obtained using Gaussian kernels with $\sigma = 10, 20, 30$. The image is of a location east of Dongsha and contains ISWs with a wide range of widths, lengths, and SSHA amplitudes, making it well suited for evaluating sensitivity to filter scale.

As shown in Figure 9, when $\sigma = 10$, the Gaussian filter has a relatively high cutoff frequency and removes the large-scale background component too aggressively, as shown in Figure 9a. This over-filtering substantially weakens ISW energy at scales comparable to the crest line width, causing some originally weak ISW signals to fall below the Otsu adaptive threshold. This is particularly evident for the crest lines within the red dashed box, which are ultimately missed completely. In contrast, when $\sigma = 30$, the smoothing scale becomes too large and fails to effectively suppress sub-mesoscale environmental background noise and the low-frequency envelope of adjacent wave packets, as shown in Figure 9c. As a result, the boundaries between different crest lines in the high-frequency SSHA field become blurred, leading to obvious under-segmentation in the black boxed region of the final result. In this case, adjacent crest lines within the same wave packet become connected and merge into coarse clusters, and their fine structural characteristics are lost. Overall, the comparison shows that the filter with $\sigma = 20$ achieves the best balance between suppressing background noise and preserving high-frequency target features. The high-frequency SSHA field extracted with this parameter, shown in Figure 9b, has a high signal-to-noise ratio, and the corresponding segmentation result not only successfully identifies the weak crest lines within the red box, but also effectively avoids the merging of multiple ISW features within the same wave packet, thereby preserving the continuity, independence, and high fidelity of the extracted crest lines.

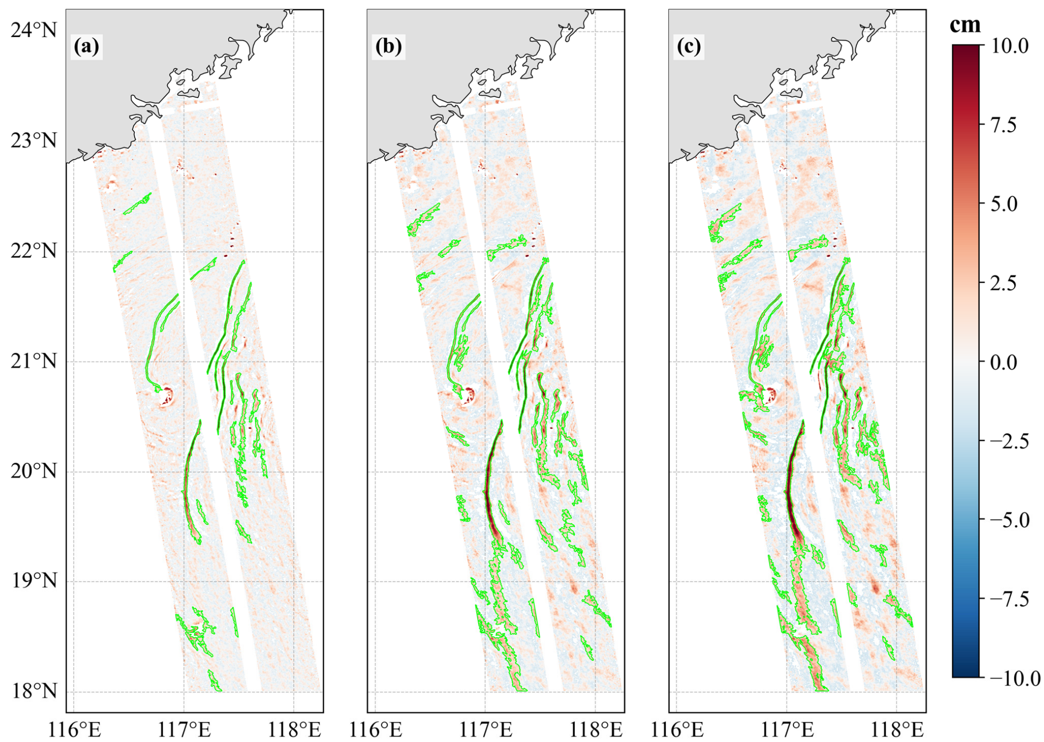

Figure 9. High-frequency SSHA component and ISW mask boundaries (green lines) segmented from the SSHA image: (**a**–**c**) correspond to the cases of $\sigma = 10, 20, 30$.

To quantitatively assess the extraction performance of the algorithm under different filter scales, radial power spectral density (PSD) analysis was introduced to compare the spectral power of SSHA signals under different σ values at typical ISW spatial scales, thereby evaluating the fidelity of the algorithm to features of different sizes. Within the typical ISW crest width range of 500 m to 2 km, the filter with $\sigma = 20$ shows the best signal fidelity. Compared with $\sigma = 10$, it causes much less attenuation of useful high-frequency information and preserves ISW features more completely. Its preservation performance is also comparable to that of $\sigma = 30$, thus providing better fidelity to ISW width as a key geometric characteristic, as shown in Figure 10a. Further residual analysis shows that, within this width range, the radial power spectral density of the high-frequency SSHA signal extracted with $\sigma = 20$ agrees closely with that of the residual signal after removal of the large-scale background, further confirming the ability of this parameter to capture key high-frequency SSHA signals, as shown in Figure 10b.

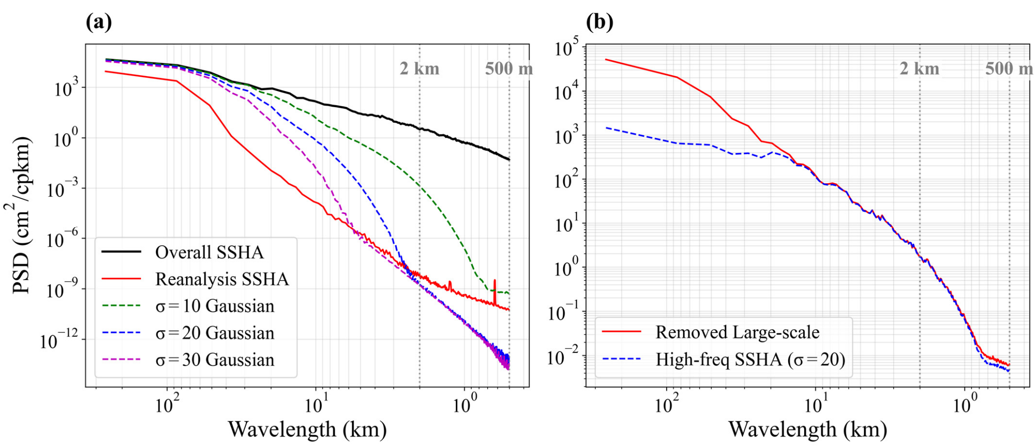

Figure 10. Effects of different Gaussian filter sizes on the radial power spectral density of SSHA signals. (**a**) Large-scale SSHA signal, and (**b**) high-frequency SSHA signal.

At the sub-mesoscale range corresponding to crest line length, approximately 10 km, $\sigma = 20$ also shows a good balance. Although this scheme still retains some large-scale energy within this range, its overall performance is clearly better than that of $\sigma = 10$. The results show that Gaussian filtering with $\sigma = 10$ suppresses sub-mesoscale signals too strongly and often causes physically unrealistic breaks in some relatively long crest lines in the high-frequency SSHA field, whereas $\sigma = 20$ is more effective in preserving the spatial coherence of crest lines. At mesoscales and larger scales, greater than 20 km, differences in the PSD of the resulting large-scale SSHA signals are small among different σ values, but all of them show stronger low-frequency noise removal than the traditional method based on subtracting the reanalysis field. Overall, choosing $\sigma = 20$ as the filtering parameter provides the best balance between suppressing the large-scale environmental background and preserving high-frequency ISW details, and supplies high-quality, high-signal-to-noise-ratio input data for subsequent morphology-based crest line extraction.

Although the present sensitivity analysis indicates that a Gaussian filtering scale of $\sigma = 20$ provides a good balance for the northern South China Sea scenes examined here, the optimal parameter setting is not expected to be universal across all SWOT SSHA scenes. In practice, the preferred smoothing scale is likely to depend on the characteristic width of the target crest structures and the level of background variability. When the ISW crest lines are relatively narrow, a smaller σ may be more suitable to avoid over-smoothing and loss of fine-scale crest features, whereas broader crest structures can tolerate, and may benefit from, a larger σ for more complete suppression of the slowly varying background. This interpretation is broadly consistent with previous ISW remote sensing studies, which have shown that crest morphology, wavelength, and packet structure vary substantially across regions and propagation stages, and that image-based extraction methods are therefore sensitive to both target scale and background conditions.

The same consideration applies to the morphology-based screening step. In scenes dominated by multi-wave interference, the superposition of high-SSHA signatures from multiple crest lines may generate locally enhanced SSHA anomaly patches so that Otsu-based thresholding retains only small, localized regions near the interference zones. Under such conditions, relaxed thresholds for the minimum connected-component area, aspect ratio, and major-axis length may help preserve physically meaningful crest fragments that would otherwise be removed as non-targets. By contrast, in scenes with more obvious background noise or without ISW crest interference, stricter morphological thresholds can be more effective in suppressing fragmented false targets and enhancing the extraction of coherent ISW structures. Therefore, although fixed parameter values are used in the present study for reproducibility and consistency, a scene-dependent tuning strategy based on local SSHA variance, crest width, or interference complexity would be a reasonable direction for future improvement.

4.2. CNR Improvement and Signal Gain Before and After High-Frequency SSHA Extraction

To further evaluate the effectiveness of high-frequency signal extraction, the CNR of SWOT SSHA images was used as the evaluation metric, and the enhancement effect was quantified by comparing CNR before and after high-frequency signal extraction. The formulas for CNR and its gain are given in Equations (13) and (14), respectively.

$$\mathrm{CNR} = \frac{\left|\mu_{fg} - \mu_{bg}\right|}{\sigma_{bg}} \tag{13}$$

$$\mathrm{Gain}_{dB} = 20\lg\frac{\mathrm{CNR}_{enhanced}}{\mathrm{CNR}_{raw}} \tag{14}$$

Here, σ_{bg} denotes the standard deviation of background pixels, CNR_{raw} denotes the CNR of the SSHA image before high-frequency component extraction, $\text{CNR}_{enhanced}$ denotes the CNR of the SSHA image after high-frequency signal extraction, and Gain_{dB} denotes the signal gain expressed in decibels (dB).

Figure 11 shows the statistical distributions of CNR and signal gain for ISW signals after applying two high-frequency component extraction methods, namely subtraction of the low-frequency component obtained with a Gaussian filter at $\sigma = 20$ and subtraction of the reanalysis SSHA background field. Overall, the raw signal, the enhanced signal, and the gain all exhibit a pronounced right-skewed distribution. Before high-frequency component extraction, 86.4% of the samples had CNR ≤ 1.0, indicating that most internal wave signals were still buried in the background noise. After processing with the method proposed in this study, CNR is significantly improved and shows stronger feature enhancement than the baseline approach that removes only the large-scale background derived from the reanalysis field. When CNR = 1.0 is used as the detection threshold, 91.7% of the samples in the baseline scheme still remain below this threshold, and the result is even worse than that before extraction, whereas the proposed method raises about 99.6% of the samples to a clearly distinguishable level, as shown in Figure 11a. In terms of gain distribution, Figure 11b shows that the proposed method provides stable and substantial enhancement. About 14.0% of the samples exhibit gains greater than 20 dB, corresponding to $\text{CNR}_{\text{enhanced}} \geq 10 \cdot \text{CNR}_{\text{raw}}$, and most samples have gains between 5 and 15 dB, with overall performance clearly superior to that of the baseline scheme. Taken together, the statistical results indicate that the proposed method effectively lifts weak ISW signals near the noise floor above the detection threshold and thus substantially improves the robustness of target identification under complex sea-state conditions.

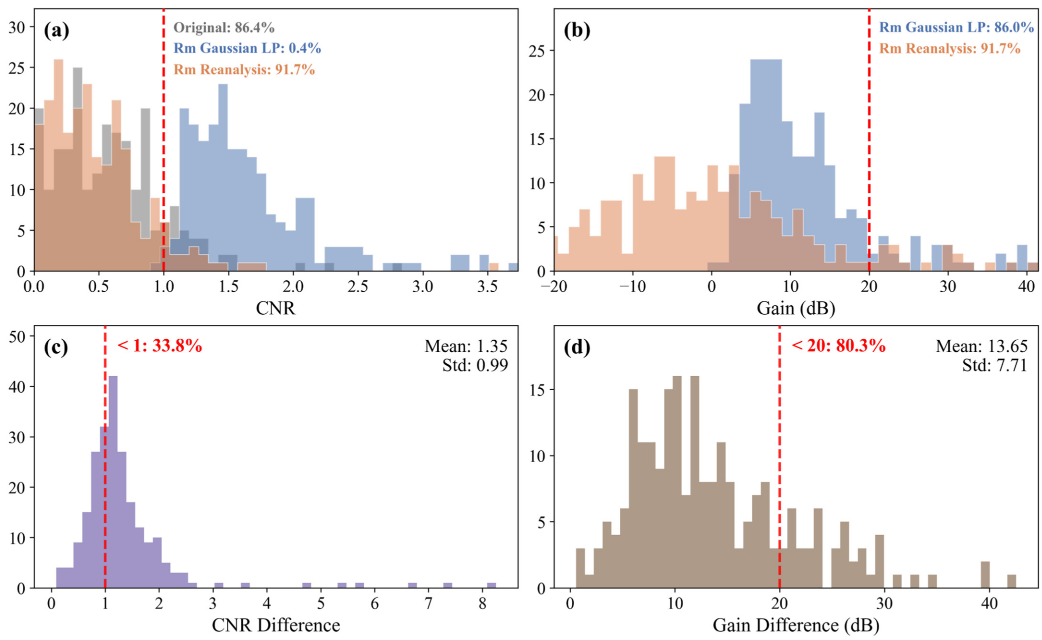

Figure 11. CNR and signal gain before and after high-frequency extraction. (**a**) CNR of the SSHA image before and after extraction, (**b**) signal gain of the SSHA image after extraction, (**c**) CNR difference between the Gaussian-filter-based method and the baseline, and (**d**) gain difference between the Gaussian-filter-based method and the baseline. The red dashed lines indicate the reference thresholds. The percentages labeled near the dashed lines denote the proportions of samples located to the left of each threshold, namely CNR < 1 in panel (**a**), gain < 20 dB in panel (**b**), CNR difference < 1 in panel (**c**), and gain difference < 20 dB in panel (**d**).

To further quantify the performance gain of the Gaussian-filter-based SSHA high-frequency component extraction method relative to the traditional reanalysis-subtraction background method, Figure 11c shows the distributions of the differences between the two schemes in CNR and signal gain. The statistical results show that the mean difference in enhanced CNR is 1.35, with a standard deviation of 0.99. Given that the CNR of the raw signal is generally below 1.0, this substantial net increase indicates that the proposed method can effectively enhance the contrast of weak ISW signals. In terms of gain difference, Figure 11d shows a clear advantage of the proposed method over the baseline scheme, with a mean difference of 13.65 dB and a standard deviation of 7.71 dB, and with nearly 20% of the samples having a gain difference greater than 20 dB. This means that, for these samples, the CNR after enhancement by the proposed method exceeds that obtained with the traditional reanalysis-subtraction method by more than a factor of 10. These results indicate that removing only the large-scale background from reanalysis data is insufficient to fully enhance the fine-scale details of high-frequency ISW signals in SWOT observations, whereas the proposed Gaussian-filter-based SSHA high-frequency component extraction method substantially improves the robustness of high-frequency ISW SSHA signal enhancement through more precise suppression of background noise.

4.3. Performance Analysis of ISW Segmentation Under Complex Oceanographic Conditions

To address the complex and highly variable dynamical environment of the northern SCS, this study further evaluated the feature extraction capability of the proposed algorithm under four typical extreme scenarios, including regions strongly affected by typhoons, regions dominated by strong instrument-induced coherent noise, shallow shelf regions, and interference zones of multiple ISW radiation fields. In the SWOT L3 Unsmoothed product, rainfall or increased significant wave height can substantially increase SWOT SSHA measurement errors and generate dense point-like noise. This type of noise often appears as a fragmented salt-and-pepper-like texture in space, and its intensity can even be comparable to that of ISW signals.

As shown in Figure 12a, under such conditions, conventional local-gradient-based edge detectors, such as the Canny or Sobel operators, tend to produce a large number of isolated false edges, causing the extracted crest lines to become fractured and fragmented and making it difficult to form physically meaningful continuous wave trains. Figure 12a shows a high-frequency SWOT SSHA image acquired on 6 September 2024. The northern nearshore part of the image lies close to Shantou and was affected by Super Typhoon Yagi. In the red-boxed region, the weather changed from moderate rain to moderate-to-heavy rain on that day, resulting in dense point-like anomalously high SSHA values. Figure 12e shows the ISWs segmented by the proposed method. The results indicate that screening based on morphological constraints, particularly aspect ratio, can effectively remove false ISW masks induced by this type of noise.

Affected by interferometric baseline roll errors and phase-system biases, some SWOT images contain coherent stripe noise that is approximately parallel to the satellite ground track, as shown in Figure 12b. This type of noise usually appears as large-scale, quasi-linear high-frequency texture, and its spatial wavenumber spectrum partially overlaps with that of submesoscale ISW signals, making it difficult to remove by Gaussian filtering. When the orientation of an ISW crest line forms a small angle with the satellite track, that is, when the two are nearly parallel, conventional algorithms based on gradient or ridge detection can easily misidentify the stripe noise as internal wave crests. This leads to a large number of spurious linear features extending across the entire image in the segmentation result and substantially reduces the accuracy of internal wave extraction. Although this stripe noise cannot be effectively removed by Gaussian filtering, its SSHA is usually much lower than that of strongly nonlinear ISWs. On this basis, the Otsu adaptive thresholding algorithm used in this study takes advantage of the bimodal characteristic of the global grayscale histogram and can automatically identify and isolate the high-SSHA internal wave signals located in the long-tail part of the histogram, thereby effectively removing low-energy coherent stripe noise, as shown in Figure 12f.

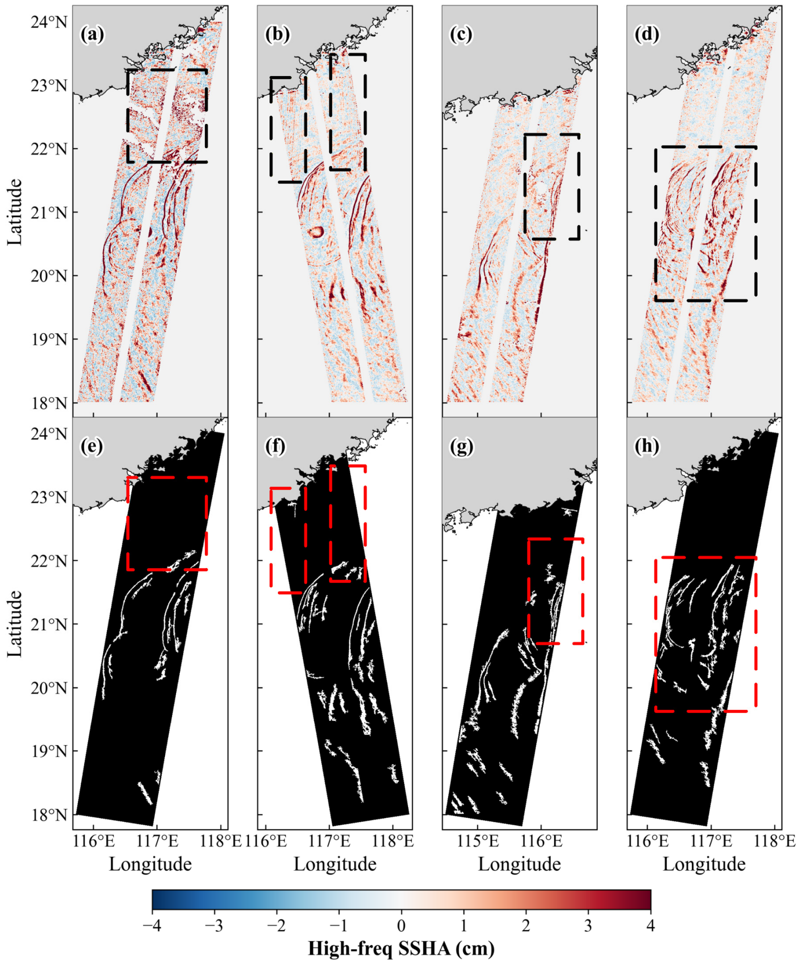

Figure 12. (**a**–**d**) High-frequency SSHA component images, with black dashed boxes marking the typical regions of (**a**) strong typhoon influence, (**b**) strong instrument noise and stripe interference, (**c**) shallow shelf water, and (**d**) multi-wave interference. Panels (**e**–**h**) show the corresponding binary ISW masks, and the red dashed boxes highlight the accurate extraction of ISW features under these complex backgrounds.

Figure 12c shows the spatial distribution of high-frequency SSHA after ISWs propagate into the shallow shelf region. When ISWs reach the shallow continental slope near Dongsha, their waveforms undergo strong transformation under the influence of nonlinear topographic effects. The wave width contracts sharply from more than 2 km in the deep basin to less than 1 km, and the wave train undergoes fission to form a dense wave packet. At this stage, the spatial scale of the wave width approaches the spatial Nyquist sampling limit of SWOT. For the Unsmoothed product, this limit is about 500 m. Meanwhile, nearshore dynamical processes make the background flow field more complex and thus increase the likelihood of missed detection of ISW signals. The red-boxed region in Figure 12g shows the extraction result for shallow-water ISW signals. The results indicate that the algorithm can fully extract the slender shallow-water ISW wave-packet structure within the red box, while the boundaries of individual crest lines remain clear and show almost no adhesion.

Figure 12d shows an interference zone of multiple ISW radiation fields observed by SWOT west of Dongsha Atoll. This pattern mainly arises from topography-induced wave–wave interactions. When large-scale ISWs propagate toward Dongsha Atoll, blockage and refraction by the atoll cause the original crest lines to break and split into two diffracted branches extending southward and northward. These two branches are then deflected and re-converge in the lee of the atoll, where phase differences generated by their different propagation paths produce strong multi-wave interference. Image segmentation in this region faces two main difficulties. First, crest line orientations are highly interlaced and local spacing is extremely small, so conventional segmentation operators tend to merge nearby or intersecting ridges into a single connected patch, causing the loss of fine-scale spatial details of high-frequency solitons within the wave packet. Second, multi-wave interference causes strong local SSHA fluctuations, enhancing some wavefront signals while making others extremely weak and fragmented, which complicates accurate tracking and complete extraction of discontinuous crest lines in the presence of instrument noise. The red-boxed region in Figure 12h shows the extraction result of the proposed method for ISW signals in this multi-wave interference zone near Dongsha. The results show that the extracted mask can effectively disentangle interwoven crest lines from multiple sources and accurately recover their deflected and overlapping spatial distribution under the topographic modulation of Dongsha Atoll. It also prevents adhesion between adjacent crest lines and preserves the physical independence and continuity of individual interference stripes. Even in the diffraction zone west of Dongsha, where ISW signals are relatively weak, the algorithm still clearly delineates slender crest line structures.

In addition to these representative background scenarios, the effect of sea-state complexity on segmentation performance is illustrated Figure 13. Panels (a–d) show the corresponding high-frequency SSHA scenes, with significant wave heights (SWHs) of 1.33 m, 1.67 m, 2.97 m, and 4.63 m, respectively, corresponding to sea states 3–6. Panels (e–h) show the associated segmentation results. Under slight to rough sea-state conditions (SWH = 1.33–2.97 m), the proposed method is still able to preserve the main geometric morphology and spatial continuity of the ISW crest lines reasonably well. This may be related to the fact that sea-state correction has already been applied in SWOT Level-3 SSHA products, so only residual sea-state bias at the centimeter level remain. However, under the most extreme case shown here, corresponding to sea-state 6, the segmentation performance degrades markedly, mainly reflected in the difficulty of preserving coherent crest line structures in the SSHA field. This suggests that under very rough sea-state conditions, the residual sea-state bias and the increased background complexity can substantially increase the difficulty of ISW crest extraction.

To further compare the proposed workflow with classical edge-based methods under noisy SWOT conditions, the paper also applies the proposed workflow and two traditional edge segmentation methods—Canny segmentation and the 2D Discrete Wavelet Transform (DWT)-based segmentation method—to high-frequency SSHA under the two typical noise-influenced environments shown in Figure 14. Overall, the method in this paper can relatively completely segment continuous ISW crest lines, while the background contains fewer discrete artifacts. In contrast, the Canny method is more prone to generating broken artifacts and almost fails to extract the crest lines; the 2D DWT-based method can segment most of the ISW crest lines but still accompanies more artifacts in complex backgrounds. These results indicate that, under complex background and noisy conditions, classical edge detection methods are more sensitive to noise, while the method in this paper is better suited for extracting ISW crest lines with continuous geometric shapes.

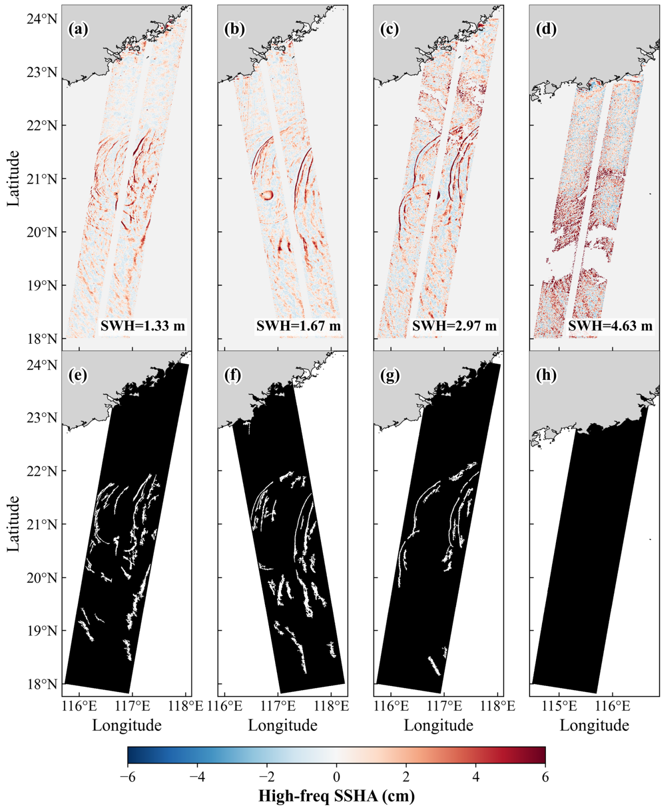

Figure 13. (**a**–**d**) High-frequency SSHA component images in different SWH. Panels (**e**–**h**) show the corresponding binary ISW masks.

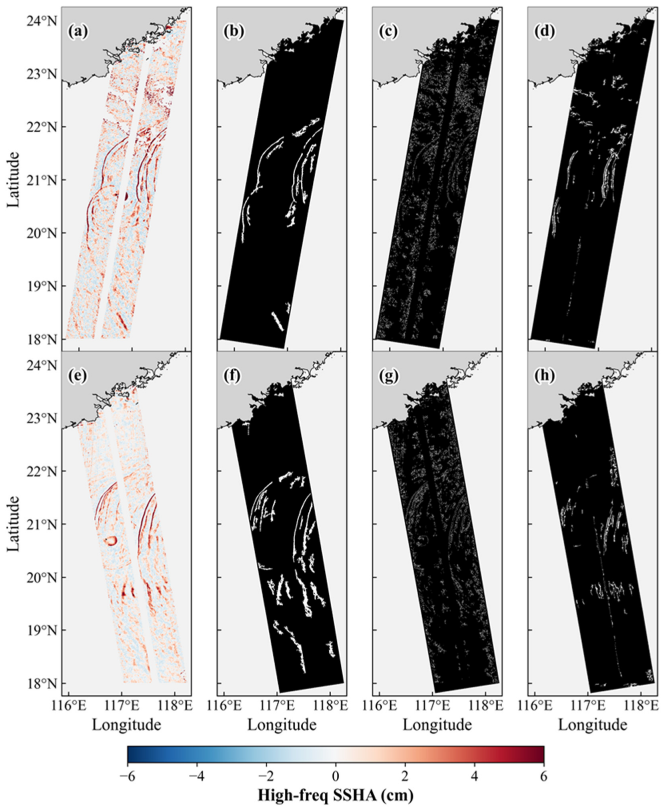

Figure 14. Representative noisy high-frequency SSHA scenes. Panels (**a**,**e**) show the input high-frequency SSHA fields. Panels (**b**,**f**) show the corresponding binary ISW masks produced by the proposed workflow. Panels (**c**,**g**) show the ISW masks obtained using the Canny method. Panels (**d**,**h**) show the ISW masks obtained using the 2D DWT-based method.

4.4. Cross-Validation with Quasi-Synchronous MODIS Imagery

To verify the physical realism and geometric accuracy of the ISW features extracted by the proposed algorithm under complex ocean backgrounds, this study used quasi-synchronous true-color optical images acquired by the Moderate Resolution Imaging Spectroradiometer (MODIS) and the Visible Infrared Imaging Radiometer Suite (VIIRS) as independent reference data sources. In these optical images, surface convergence and divergence induced by ISWs strongly modulate sea surface roughness and produce clear bright–dark banding patterns, allowing relatively accurate identification of the leading crest and trailing wave train of each ISW packet. The MODIS and VIIRS images used in this study were acquired at 10:15 on 12 April 2024 and 13:00 on 8 July 2024, respectively. The corresponding SWOT overpass times were 12:25:40 and 10:36:19 on the same days, both in Beijing time, and the observation time differences were approximately $\Delta t \approx 2.18$ and $\Delta t \approx -2.4$, respectively.

As shown in Figure 15a,c, in the case of 12 April 2024, the MODIS image was acquired about 2.18 h earlier than the SWOT overpass. Because the ISWs propagated persistently toward the northwest, the high-frequency SSHA crest lines extracted from SWOT (red pixels) were located systematically ahead of the optical wave signatures. The two were nearly parallel in planform, with an average offset of about 15.3 km. Based on the time difference and spatial offset, the mean phase speed of the wave packet is estimated to be about 1.968 m/s, consistent with the typical propagation speed of ISWs in the deep basin of the northern SCS. Figure 15b,d show the results for 8 July 2024. In this case, the SWOT overpass occurred about 2.4 h earlier than the VIIRS image acquisition. Under this lead-observation condition, the SSHA crest lines identified by SWOT were located behind the optical stripes, on their southeastern side, with an average offset of about 10.6 km. The corresponding phase speed was about 1.227 m/s, which is also consistent with the typical propagation speed of ISWs near Dongsha.

Comprehensive comparison shows that the crest lines extracted by the proposed algorithm from SWOT SSHA data are highly consistent with the morphologies revealed by optical imagery in terms of fine-scale characteristics such as geometric structure, curvature variation, and intra-packet spacing. More importantly, under two opposite time-offset conditions, the extracted results both exhibit spatial displacement directions consistent with the physical propagation logic. This strongly indicates that the high-frequency SSHA crest lines identified by the algorithm correspond to real ISW features rather than coherent noise or artifacts, thereby confirming the reliability of the algorithm in the task of ISW segmentation.

4.5. Segmentation Performance in Andaman Sea

To further evaluate the applicability of the proposed workflow in a different ocean basin, SWOT Unsmoothed L3_LR_SSH products over the Andaman Sea (Spatial coverage: 92°E–99°E and 5°N–16°N) from March 2024 to March 2025 were also collected, and ISW crest lines were extracted following the workflow proposed in this study. Figure 16 presents the ISW segmentation results derived from SWOT high-frequency SSHA images acquired on 23–25 March and 24–26 April 2024, covering nearly the entire Andaman Sea. The results suggest that there are five major hotspot regions of ISW activity in the basin, denoted as S1–S5.

In the northern Andaman Sea, the ISW crest lines associated with S1 mainly propagate southeastward and can extend toward the continental shelf along the Myanmar coast, whereas those associated with S2 mainly propagate southwestward. This pattern is consistent with previous descriptions of the two dominant ISW propagation types in the northern Andaman Sea, namely type-SE and type-SW.

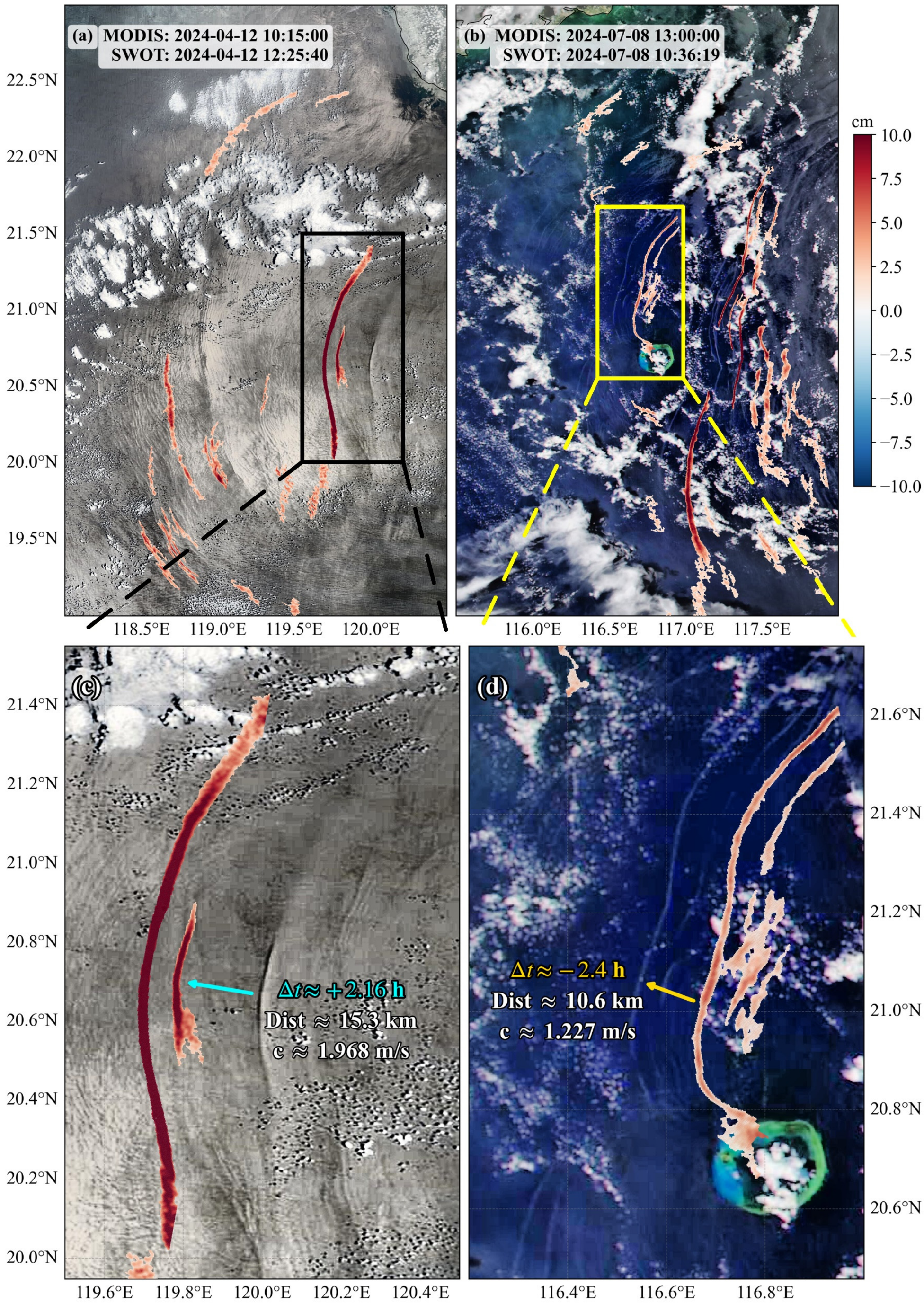

Figure 15. Comparison between crest line stripes in MODIS and VIIRS true-color images at different times and the crest lines extracted from SWOT SSHA. Panels (**a**,**c**) show the MODIS image and the corresponding enlarged region on 12 April 2024; panels (**b**,**d**) show the VIIRS image and the corresponding enlarged region on 8 July 2024. The dashed boxes indicate the enlarged regions shown in panels (**c**) and (**d**), respectively.

In the central Andaman Sea, the source regions S3 and S4 are located near the Nicobar Islands. The ISWs generated there exhibit a clear bidirectional propagation pattern: the westward-propagating waves extend toward the southern Bay of Bengal, while the eastward-propagating waves move toward the continental shelves of Myanmar and Thailand. During propagation, the crest lines generated from S3 and S4 can intersect and interfere with one another, although their overall propagation directions remain largely unchanged.

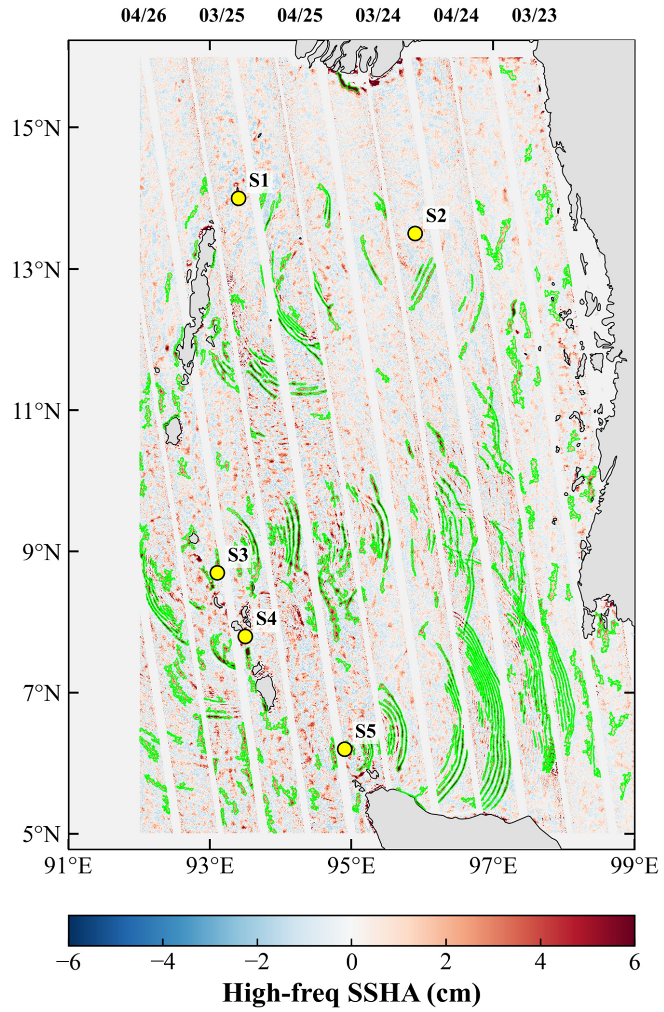

Figure 16. High-frequency SSHA component and ISW mask boundaries (green lines) segmented from the SSHA image covering the Andaman Sea. Hotspots S1–S5 are denoted as yellow circles.

S5 is in the southern Andaman Sea near Sumatra. The ISWs generated from this region mainly propagate eastward and appear in the SWOT high-frequency SSHA images as densely packed wave trains. These crest lines extend roughly from 5°N to 9°N. Compared with the ISWs in the northern and central parts of the basin, the southern wave trains generally contain more crest lines, and in some cases, wave packets composed of more than ten crests can be observed.

5. Conclusions

In this study, we developed an ISW segmentation method for SWOT SSHA imagery by combining Gaussian filtering with morphological processing, and systematically evaluated its performance under different topographic and hydrodynamic conditions. First, using CNR and signal gain as evaluation metrics, we compared the Gaussian-filter-based high-frequency SSHA extraction method with the traditional scheme based on reanalysis background fields. Second, we examined the screening effect of the morphological algorithm on the preliminary Otsu segmentation results to determine whether it can effectively preserve real ISW connected components. The robust segmentation performance of the algorithm under various extreme conditions further demonstrates its reliability. Finally, quasi-synchronous optical imagery was used to cross-validate the ISW connected components extracted by the algorithm and to verify their physical realism. The main conclusions of this study are summarized below.

- Compared with the baseline method that extracts high-frequency SWOT SSHA by subtracting a reanalysis background field, the Gaussian low-pass-filter-based background removal scheme proposed in this study shows significant and stable enhancement across all samples. The mean CNR improvement is 1.35 with a standard deviation of 0.99, and the mean signal-gain improvement is 13.65 dB with a standard deviation of 7.71 dB, indicating that the proposed method outperforms the baseline for most samples.
- Morphological constraints can effectively suppress false detections produced by Otsu threshold segmentation. In shelf regions where ISW signals are weak, crest widths are narrow, and multiple crest lines interfere with one another, causing discontinuous crest patterns, the selected parameter combination, namely connected-component area > 300 pixels, major-axis length > 100 pixels, and aspect ratio > 6, effectively constrains the preliminary Otsu segmentation results. It substantially removes speckle noise and fragmented artifacts while preserving slender real crest structures.
- The proposed ISW segmentation algorithm successfully extracts crest lines consistent with the expected geometric morphology in three typical regions, including the deep basin, continental slope, and continental shelf. Beyond these typical regions, the algorithm also maintains high robustness under four extreme scenarios, namely waters affected by super typhoons, images contaminated by strong instrument-induced interference noise, shallow shelf regions, and multi-wave interference zones, thereby providing reliable support for large-scale ISW extraction.
- Comparison between quasi-synchronous optical imagery and SWOT SSHA segmentation results shows that, whether the optical image is acquired earlier or later than the SWOT overpass, the ISW crest lines extracted from SWOT remain nearly parallel to the corresponding crest lines in the optical imagery. Propagation speeds estimated from the spatial offsets and time intervals between the two observations are also consistent with previous studies. This indicates that the ISW crest lines extracted by the proposed algorithm correspond to real ISW features rather than artifacts, thus providing independent external evidence for the validity of the segmentation results.

In summary, this study proposes an automatic ISW segmentation framework for SWOT L3 LR Unsmoothed SSHA data. The framework extracts high-frequency SSHA by subtracting a Gaussian-filtered background from the preprocessed SSHA field and combines Otsu automatic thresholding with morphological constraints to achieve robust ISW segmentation across different regions and multiple extreme scenarios in the northern SCS. In addition to its value as a workflow for SWOT SSHA image processing, this method also provides a practical observational basis for future studies on ISW tracing, topographic modulation, and the interactions of ISW with other dynamic phenomena such as the Kuroshio and mesoscale eddies based on 2D SWOT SSHA data. At the same time, current validation is still limited to the northern South China Sea and parts of the Andaman Sea, and the broader applicability of this framework in other sea areas and environmental conditions still needs further assessment. It also should be noted that the Gaussian filter scale σ and the thresholds used in the morphological constraints still need to be selected manually, and the segmentation of ISWs in the nearshore shallow-water dissipation stage still has room for improvement. Future work will incorporate more SWOT data to evaluate the performance of this method in high-frequency SSHA enhancement and ISW segmentation across different seas, and will explore adaptive parameter selection based on regional ISW characteristics, thereby further improving the completeness and generalizability of the algorithm and its capacity to support early warning for marine engineering facilities.

https://doi.org/10.3390/rs18101463

Author Contributions: Conceptualization, P.C.; methodology, P.C.; software, P.C.; validation, P.C., J.G., Y.H. and R.X.; formal analysis, J.G., J.H. and L.J.; investigation, J.H. and L.J.; data curation, J.H., L.J., B.Z., H.Z. and S.G.; writing—original draft, P.C.; writing—review & editing, J.G.; visualization, P.C., Y.H., R.X., Y.L., Y.C. and X.R.; supervision, X.X.; project administration, X.X.; funding acquisition, X.X. All authors have read and agreed to the published version of the manuscript.

Funding: This research received no external funding.

Data Availability Statement: SWOT Unsmoothed L3_LR_SSH v2.0.1 data used in this study are publicly available from the AVISO ocean products repository (https://doi.org/10.24400/527896/A01-2024.003). Global Ocean Gridded L4 Sea Surface Heights and Derived Variables Nrt product are available in Copernicus Marine Service (https://doi.org/10.48670/moi-00145). ERA5 SWH hourly data are available in Climate Data Store (https://doi.org/10.24381/cds.adbb2d47). Because future SWOT product releases may include changes in calibration, quality flags, noise characteristics, or correction schemes, the parameter settings and segmentation performance of the proposed workflow should be re-evaluated when applying it to newer SWOT product versions. The custom code used for preprocessing, segmentation, and analysis is available from the corresponding author upon reasonable request.

Conflicts of Interest: The authors declare no conflict of interest.

References

1. Jackson, C. *An Atlas of Internal Solitary-like Waves and Their Properties*, 2nd ed.; Global Ocean Associates: Alexandria, VA, USA, 2004; p. 560.
2. Bogucki, D.; Dickey, T.; Redekopp, L. Sediment resuspension and mixing by resonantly generated internal solitary waves. *J. Phys. Oceanogr.* **1997**, *27*, 1181–1196. [CrossRef]
3. Dong, J.; Zhao, W.; Chen, H.; Meng, Z.; Shi, X.; Tian, J. Asymmetry of internal waves and its effects on the ecological environment observed in the northern South China Sea. *Deep-Sea Res. Part I Oceanogr. Res. Pap.* **2015**, *98*, 94–101. [CrossRef]
4. Wang, Y.H.; Dai, C.F.; Chen, Y.Y. Physical and ecological processes of internal waves on an isolated reef ecosystem in the South China Sea. *Geophys. Res. Lett.* **2007**, *34*, L18609. [CrossRef]
5. Farmer, D.; Alford, M.; Lien, R. From Luzon Strait to Dongsha Plateau: Stages in the Life of an Internal Wave. *Oceanography* **2011**, *24*, 64–77. [CrossRef]
6. Jackson, C. Internal wave detection using the Moderate Resolution Imaging Spectroradiometer (MODIS). *J. Geophys. Res. Ocean.* **2007**, *112*, C11012. [CrossRef]
7. Zhao, Z.; Alford, M.H.; Lien, R.-C. Source and propagation of internal solitary waves in the northeastern South China Sea. *J. Geophys. Res. Ocean.* **2006**, *111*, C11012. [CrossRef]
8. Guo, C.; Chen, X. A review of internal solitary wave dynamics in the northern South China Sea. *Prog. Oceanogr.* **2014**, *121*, 7–23. [CrossRef]
9. Ramp, S.R.; Tang, T.Y.; Duda, T.F. Internal solitons in the northeastern South China Sea part I: Sources and deep water propagation. *IEEE J. Ocean. Eng.* **2004**, *29*, 1157–1181. [CrossRef]
10. Zhao, Z.; Liu, B.; Li, X. Internal solitary waves in the China seas observed using satellite remote-sensing techniques: A review and perspectives. *Int. J. Remote Sens.* **2014**, *35*, 3926–3946. [CrossRef]
11. da Silva, J.C.B.; Ermakov, S.A.; Robinson, I.S.; Jeans, D.R.G.; Kijashko, S.V. Role of surface films in ERS SAR signatures of internal waves on the shelf: 1. Short-period internal waves. *J. Geophys. Res. Ocean.* **1998**, *103*, 8009–8031. [CrossRef]
12. da Silva, J.C.B.; Ermakov, S.A.; Robinson, I.S. Role of surface films in ERS SAR signatures of internal waves on the shelf: 3. Mode transitions. *J. Geophys. Res. Ocean.* **2000**, *105*, 24089–24104. [CrossRef]
13. Magalhaes, J.M.; da Silva, J.C.B. Internal Solitary Waves in the Andaman Sea: New Insights from SAR Imagery. *Remote Sens.* **2018**, *10*, 861. [CrossRef]
14. Jackson, C.R.; da Silva, J.C.B.; Jeans, G.; Alpers, W.; Caruso, M.J. Nonlinear internal waves in synthetic aperture radar imagery. *Oceanography* **2013**, *26*, 68–79. [CrossRef]
15. Hu, Z.; Yu, F.; Lv, H.; Chen, G. ST-multi-ISWNet: An internal solitary wave instance segmentation algorithm based on spatial-temporal multi-modal under high sea states. *Int. J. Digit. Earth* **2026**, *19*, 2640693. [CrossRef]
16. Brandt, P.; Romeiser, R.; Rubino, A. On the determination of characteristics of the interior ocean dynamics from radar signatures of internal solitary waves. *J. Geophys. Res. Ocean.* **1999**, *104*, 30039–30045. [CrossRef]
17. Araujo, I.B.; da Silva, J.C.B.; Ermakov, S.A.; Robinson, I.S. On the role of wind direction in ERS SAR signatures of internal waves on the Iberian shelf. *Glob. Atmos. Ocean Syst.* **2002**, *8*, 269–291. [CrossRef]

18. Huang, L.; Yang, J.; Ma, Z.; Liu, B.; Ren, L.; Liu, A.K.; Chen, P. High-Frequency Observations of Oceanic Internal Waves from Geostationary Orbit Satellites. *Ocean-Land-Atmos. Res.* **2023**, *2*, 0024. [CrossRef]
19. Otsu, N. A Threshold Selection Method from Gray-Level Histograms. *IEEE Trans. Syst. Man Cybern.* **1979**, *9*, 62–66. [CrossRef]
20. Matthews, J. Stereo observation of lakes and coastal zones using ASTER imagery. *Remote Sens. Environ.* **2005**, *99*, 16–30. [CrossRef]
21. Chust, G.; Sagarminaga, Y.; Borja, Á.; Franco, J.; Uriarte, A. The multi-angle view of MISR detects oil slicks under sun glint conditions. *Remote Sens. Environ.* **2007**, *107*, 232–239. [CrossRef]
22. Feng, L.; Hu, C.; Lee, Z.; Cannon, S.; Zhao, X.; Kowalewski, M.G. Cloud and sun-glint statistics derived from GOES and MODIS observations over the Intra-Americas Sea for GEO-CAPE mission planning. *J. Geophys. Res. Atmos.* **2017**, *122*, 1725–1742. [CrossRef]
23. Santos-Ferreira, A.M.; Da Silva, J.C.B.; Magalhaes, J.M. SAR Mode Altimetry Observations of Internal Solitary Waves in the Tropical Ocean Part 1: Case Studies. *Remote Sens.* **2018**, *10*, 644. [CrossRef]
24. Santos-Ferreira, A.M.; Da Silva, J.C.B.; Srokosz, M. SAR-Mode Altimetry Observations of Internal Solitary Waves in the Tropical Ocean Part 2: A Method of Detection. *Remote Sens.* **2019**, *11*, 1339. [CrossRef]
25. Qiu, B.; Chen, S.; Wang, J.; Fu, L.-L. Seasonal and Fortnight Variations in Internal Solitary Waves in the Indonesian Seas From the SWOT Measurements. *J. Geophys. Res. Ocean.* **2024**, *129*, e2024JC021086. [CrossRef]
26. Dibarboure, G.; Anadon, C.; Briol, F.; Cadier, E.; Chevrier, R.; Delepoulle, A.; Faugère, Y.; Laloue, A.; Morrow, R.; Picot, N.; et al. Blending 2D topography images from SWOT into the altimeter constellation with the Level-3 multi-mission DUACS system. *EGUsphere* **2024**, *2024*, 1–64. [CrossRef]
27. Zhang, E.; Miao, M.; Zhang, Z. Exploring Submesoscale Processes and Internal Solitary Waves Using SWOT Data in the South China Sea. *J. Geophys. Res. Ocean.* **2025**, *130*, e2025JC022700. [CrossRef]
28. da Silva, J.C.B.; Magalhaes, J.M.; Bosser, A.; Huerre, R.; Koch-Larrouy, A.; Goret, C.; Diallo, S.; de Macedo, C.R.; da Silva, A.C. Internal solitary wave parameters from SWOT KaRIn sea surface topography: A case study in the Tropical Atlantic. *Sci. Remote Sens.* **2025**, *12*, 100307. [CrossRef]
29. Pan, Z.; Zhai, Z.; Li, Q.; Li, Q.; Wu, L.; Bao, L. Preliminary Investigation of the Spatial-Temporal Characteristics and Vertical Dynamics of Internal Solitary Waves in the South China Sea from SWOT Data. *J. Mar. Sci. Eng.* **2025**, *13*, 304. [CrossRef]
30. Zhang, H.; Fan, C.; Huang, L.; Sun, L.; Meng, J. SWOT-Based Detection of Sea Surface Height Variations Induced by Internal Solitary Waves: Feature Extraction and Amplitude Inversion. *IEEE J. Sel. Top. Appl. Earth Obs. Remote Sens.* **2026**, *19*, 805–814. [CrossRef]
31. Wang, T.; Huang, X.; Yang, Y.; Huang, S.; Zhou, C.; Zhao, W.; Tian, J. Three-Dimensional Evolution of Internal Solitary Waves in the Northern South China Sea Revealed by SWOT Observations. *J. Geophys. Res. Ocean.* **2025**, *130*, e2025JC023050. [CrossRef]
32. Goret, C.; Koch-Larrouy, A.; Kouogang, F.; de Macedo, C.R.; M'Hamdi, A.; Magalhaes, J.M.; da Silva, J.C.B.; Tchilibou, M.; Artana, C.; Dadou, I.; et al. Internal solitary waves refraction and diffraction from interaction with eddies off the Amazon Shelf from SWOT. *Ocean Sci.* **2026**, *22*, 679–698. [CrossRef]
33. Rodenas, J.A.; Garello, R. Wavelet analysis in SAR ocean image profiles for internal wave detection and wavelength estimation. *IEEE Trans. Geosci. Remote Sens.* **1997**, *35*, 933–945. [CrossRef]
34. Zheng, Y.-g.; Zhang, H.-s.; Wang, Y.-Q. Stripe detection and recognition of oceanic internal waves from synthetic aperture radar based on support vector machine and feature fusion. *Int. J. Remote Sens.* **2021**, *42*, 6706–6724. [CrossRef]
35. Vasavi, S.; Divya, C.; Sarma, A.S. Detection of solitary ocean internal waves from SAR images by using U-Net and KDV solver technique. *Glob. Transit. Proc.* **2021**, *2*, 145–151. [CrossRef]
36. Cui, G.; Cai, Z.; Yang, X. IWResNet-MA: A deep learning framework for extracting internal wave stripe and propagation direction from SAR imagery. *Ocean Eng.* **2025**, *328*, 121030. [CrossRef]
37. Shi, Y.; Meng, J.; Zhao, J.; Long, R.; Sun, L.; Zhang, Z. Crest extraction of internal solitary waves from synthetic aperture radar images based on an improved segformer model. *J. Appl. Remote Sens.* **2026**, *20*, 014507. [CrossRef]
38. Zhang, X.; Li, X. Constructing a 22-year internal wave dataset for the northern South China Sea: Spatiotemporal analysis using MODIS imagery and deep learning. *Earth Syst. Sci. Data* **2024**, *16*, 5131–5144. [CrossRef]